

Skyrmion dynamics in moiré magnets

P. S. Shaban ¹, I. S. Lobanov ¹, V. M. Uzdin ¹ and I. V. Iorsh ^{1,2,*}

¹*Department of Physics, ITMO University, St. Petersburg, 197101, Russia*

²*Abrikosov Center for Theoretical Physics, MIPT, Dolgoprudnyi, Moscow Region 141701, Russia*



(Received 12 August 2023; revised 8 October 2023; accepted 7 November 2023; published 28 November 2023)

We consider a twisted magnetic bilayer subject to the perpendicular electric field. The interplay of induced Dzyaloshinskii-Moriya interaction and spatially varying moiré exchange potential results in complex noncollinear magnetic phases in these structures. We numerically demonstrate the coexistence of intralayer skyrmions and bound interlayer skyrmion pairs and show that they are characterized by distinct dynamics under the action of external in-plane electric field. Specifically, we demonstrate the riling behavior of skyrmions along the domain walls which could find applications in spintronic devices based on van der Waals magnets.

DOI: [10.1103/PhysRevB.108.174440](https://doi.org/10.1103/PhysRevB.108.174440)

I. INTRODUCTION

van der Waals (vdW) materials offer unprecedented opportunities to form heterostructures of different monolayers with unique magnetic, transport, and optical properties and enable a powerful toolbox for bottom-up material engineering [1,2].

vdW magnets are a class of the vdW materials [3,4]. The experimental realization of two-dimensional (2D) vdW magnets CrI₃ [5] and CrGeTe₃ [6] was reported, and since then, the family of 2D magnets has rapidly grown with dozens of materials appearing each year [7]. Due to atomic-scale thickness, vdW magnets are highly susceptible to external perturbations such as external fields [8–10] and strain [11,12]. Specifically, a perpendicular electric field may induce the Dzyaloshinskii-Moriya interaction (DMI) which leads to the emergence of noncollinear magnetic structures [13] such as helices, individual skyrmions, and skyrmion crystals [14]. Moreover, for some vdW materials, their magnetic properties depend crucially on stacking configuration: Controlling the stacking angle and relative displacement of individual magnetic monolayers allows for the precise tuning of the interlayer exchange coupling (IEC) as well as dipole-dipole interaction which results in the emergence of various magnetic phases in twisted vdW magnets [15–21]. The existence of coupled skyrmionic states was predicted in twisted bilayer graphene for certain values of model parameters [22].

In twisted magnetic bilayers, the site-dependent interlayer exchange potential, or moiré potential, which is periodic with a period equal to the moiré supercell, defines the spatial scale of the emergent noncollinear phases. At the same time, the chiral interactions such as DMI correspond to an alternative spatial scale which can be tuned by external perpendicular electric fields. It is thus tempting to explore the emergent magnetic phases in twisted magnetic bilayers where both interlayer exchange moiré potential and intralayer DMI are present. Such a competition would lead to a rich phase diagram of such structures, if the strength and characteristic

length scale of two types of interactions are compatible [23]. A similar competition of intra- and interlayer interactions takes place in synthetic antiferromagnets (SAFs) [24]. In these structures, two magnetic layers are exchange-coupled through a thin metal nonmagnetic spacer due to the Ruderman-Kittel-Kasuya-Yosida (RKKY) interaction of conduction electrons. The magnitude and sign of the IEC depend on the thickness of the nonmagnetic interlayer, which can be chosen in such a way as to ensure antiferromagnetic (AFM) exchange. If in one of the magnetic layers there are domains with different directions of magnetization, then in the other layer, the same domain structure will be repeated but with the opposite direction of magnetization.

The IEC varies depending on the thickness of the spacer layer. If it is made in the form of a wedge, then the IEC will oscillate with thickness, which will lead to the formation of a domain structure, even if one of the magnetic films is in a single-domain state. Such a smooth change in thickness makes it possible to observe short- and long-range IEC oscillations in metal magnetic trilayers [25]. If, in the presence of DMI, localized magnetic structures of the skyrmion type are formed in one magnetic layer, then another skyrmion should form in the second layer, which will be in a bound state with the first one [26]. The skyrmions will be coupled ferromagnetically (FM) or AFM, and this bonding should also vary with the thickness of the nonmagnetic interlayer.

An important aspect of the physics of vdW magnets is related to their stability with respect to thermal fluctuations and random external perturbations. For SAFs, it has been experimentally shown that skyrmions in them can be stable up to room temperature [26]. Calculations within the framework of the transition state theory show that skyrmion pairs caused by interlayer interaction are more stable than individual skyrmions in layers. Moreover, it turns out that the most likely mechanism for the decay of a skyrmion pair occurs through the disappearance of the skyrmion in one of the layers [27]. The same behavior should be observed in twisted vdW magnetic layers.

In this paper, we present the features of the magnetic structure and dynamics of skyrmions in a moiré magnet

*i.iorsh@metalab.ifmo.ru

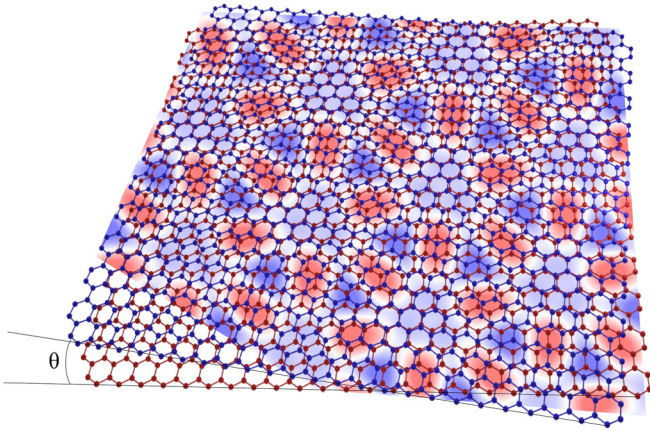


FIG. 1. Twisted ferromagnetic bilayer. Two-dimensional (2D) color map demonstrates interlayer interaction potential (moiré potential). Moiré period is proportional to a/θ , a is the lattice period, and θ is the angle between twisted layers. Twist angle on the picture is much bigger than the real moiré angle in simulations and used for better visual perception.

associated with the competition of in-plane and out-of-plane interactions. We consider the structure shown in Fig. 1. A twisted magnetic bilayer is subject to an external electric field inducing intralayer DMI in each layer. The interlayer moiré potential arises due to the spatially dependent IEC. The system models the recently reported experiments with twisted monolayers of CrI₃ [28,29]. We start from numerical modeling of the magnetic phases supported by this structure. We show that spatially dependent interlayer exchange potential results in complex noncollinear magnetic structures and the formation of FM and AFM domains. Moreover, we show that the system supports several types of intralayer skyrmions as well as bound interlayer skyrmion pairs predicted previously [17]. We then study the skyrmion dynamics using the Landau-Lifshitz-Gilbert (LLG) equation and demonstrate the raiting of skyrmions along the domain walls under the action of an external in-plane electric field. We give a qualitative explanation of the observed effect using the Thiele equation.

This paper is organized as follows: in Sec. II, we define the model and present the results of numerical simulations of the magnetic phases supported by the structure. In Sec. III, we present the results on the dynamics of the skyrmions under the external in-plane electric field. Section IV summarizes the obtained results.

II. NONCOLLINEAR MAGNETIC PHASES IN TWISTED MAGNETIC BILAYER

A. Model

In our model, we consider two layers of a FM material with a hexagonal crystal lattice, rotated relative to each other by a small angle, which determines the shape of the moiré potential. In the FM case considered below, the interaction potential is rather difficult to describe analytically, but it can be specified numerically. The moiré period is proportional to a/θ , and a is the lattice period, which is typically about several angstroms. The twist angle we use in our calculations

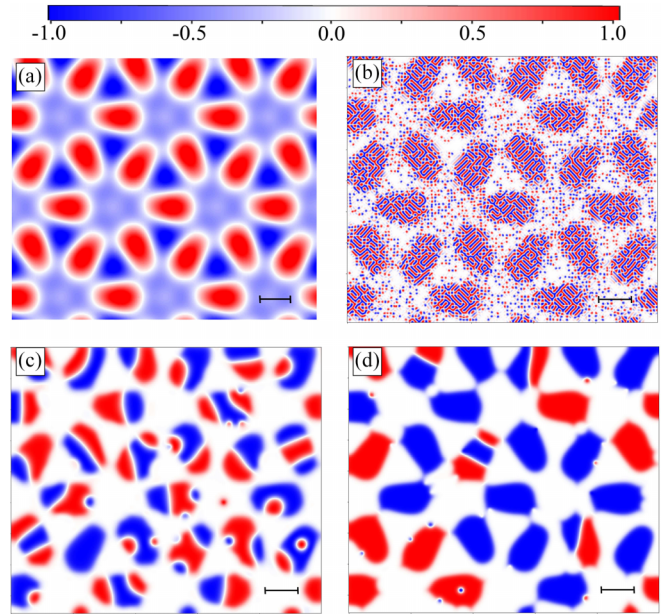


FIG. 2. (a) Spatial dependence of interlayer interaction $\Phi(\mathbf{r})$ and normalized z projection of total bilayer magnetic moments in moiré magnets for (b) $\zeta = 10$, (c) $\zeta = 1.22$, and (d) $\zeta = 0.78$. Scale bar: 100 lattice constants.

equals $\sim 0.7^\circ$. The profile of moiré potential $\Phi(\mathbf{r})$ adopted from Ref. [30] is shown in Fig. 2(a) along with a scale bar.

We consider a continuous generalized Heisenberg-type model with the energy:

$$E = d \cdot \int d^2\mathbf{r} \left(\sum_{i=1,2} \{ \mathcal{A}[\nabla\mathbf{n}_i(\mathbf{r})]^2 - \mathcal{K}n_{zi}^2(\mathbf{r}) + \mathcal{D}\mathbf{n}_i(\mathbf{r}) \cdot (\hat{\mathbf{z}} \times \nabla) \times \mathbf{n}_i(\mathbf{r}) \} - J_{1,2}\Phi(\mathbf{r})\mathbf{n}_1(\mathbf{r}) \cdot \mathbf{n}_2(\mathbf{r}) \right) \quad (1)$$

Here, \mathbf{n}_1 and \mathbf{n}_2 are the unit vectors along the magnetization in layers 1 and 2, respectively, d is the magnetic layer thickness, and \mathcal{A} is the exchange stiffness constant. Pairs of nearest atoms in different layers also contribute to the Heisenberg exchange, but the interaction strength depends on the position of atoms and equals $J_{1,2}\Phi(\mathbf{r})$, where $J_{1,2}$ is a parameter controlling the interaction strength.

DMI is turned on in each layer, but there is no antisymmetric exchange interaction between layers. Dzyaloshinskii vectors are parallel to the line connecting interacting spins; the length of the vector determines the DMI density \mathcal{D} . Anisotropy axis \mathbf{e}_z is the same for all points of the system, the anisotropy density $\mathcal{K} > 0$ corresponds to the easy-axis anisotropy. The spin texture generated in a moiré supercell can give rise to an electric polarization associated with such a noncollinear magnetic state due to spin-orbit coupling, resulting in a local ferroelectric order following moiré [31].

When performing numerical calculations, the micromagnetic model is discretized on a square lattice. A cell of 429×50 lattice points with free boundary conditions was used. Its size coincided with the cell size in Ref. [30], where the moiré potential is taken from.

Micromagnetic parameters are converted into the discrete model parameters:

$$J = 2\mathcal{A}, \quad D = a\mathcal{D}, \quad K = a^2\mathcal{K}, \quad (2)$$

where a is the in-plane lattice constant.

In our modeling, we use dimensionless variables, and all parameters in Eq. (2) are measured in J units. The easy-axis anisotropy $K/J = 0.01$ is used below, which gives an estimate of ~ 22 lattice constants for the thickness of a domain wall in a bulk material without DMI: $L = \pi\sqrt{\mathcal{A}/\mathcal{K}}$.

DMI can be varied by changing the external electric field [13], so the system will be considered at different values of the DMI constant. In a bulk material with DMI, the FM state becomes unstable with respect to the transition to the spiral state at $D_s = 4\sqrt{\mathcal{A}\mathcal{K}}/\pi$. We will use the dimensionless parameter $\zeta = D/D_s$.

B. Results

The determination of the magnetic configuration corresponding to the local energy minimum begins from a state with a random distribution of magnetic moment directions. The nonlinear conjugate gradient method is used for energy minimization with Hessian matrix evaluated in Cartesian coordinates [32]. The minimization stops when the gradient becomes $< 10^{-5}$. The system has many metastable states with close energies, and Fig. 2 reproduces the typical examples of locally stable magnetic configurations for different values of the ζ parameter. Figure 2(a) shows the spatial configuration of the moiré potential, which defines the regions with FM and AFM IEC. The interlayer exchange potential was computed in Ref. [30]. Here, $\Phi(\mathbf{r}) = 1$ (red) and $\Phi(\mathbf{r}) = -1$ (blue) correspond to the FM and AFM exchanges, respectively, and the white lines are the FM grain boundaries, where the exchange is close to zero.

For $\zeta = 10$, the ground state in each layer is a spiral structure of the fingerprint type. In the FM IEC region, the same structure is observed for the total magnetization of both layers, as can be seen from Fig. 2(b). In the AFM region, the magnetizations of the helical domains are largely compensated, except for the ends of the domains, where point out-of-plane magnetic states appear for total magnetization. These states, however, are not layer-localized structures, and their mobility is very limited since their movement can only arise as a result of rearrangement of the helical structure in each layer. We provide a more detailed illustration of the formation of these pointlike states arising due to the superposition of the domain walls in the two layers in Appendix A.

As effective DMI strength ζ decreases, the size of the domains increases. For example, at $\zeta = 1.22$ shown in Fig. 2(c), the domain size is comparable with the moiré grain size. Moreover, the skyrmion states are identified in FM and AFM regions and at the boundaries between FM and AFM.

For $\zeta = 0.78$, the observed skyrmions have size much smaller than the regions of a constant IEC sign. Figure 2(d) indicates that most of these skyrmions are located at the boundary of the moiré grains, although they also can be found inside the grains. The magnetization profiles for other values of ζ are shown in Appendix A, illustrating gradual increase of the domain size with the decrease of ζ .

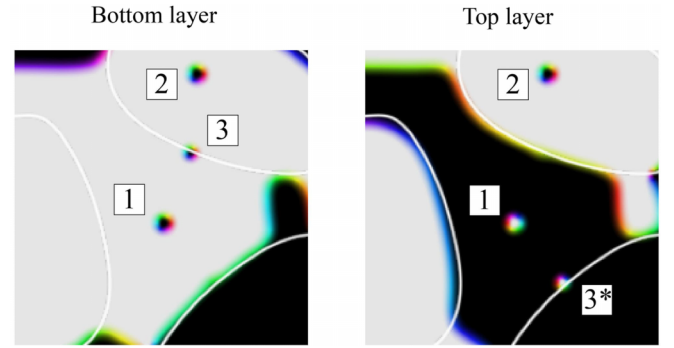


FIG. 3. Various types of skyrmions in a twisted bilayer. Light gray corresponds to the direction of the magnetization vector out-of-plane, and z component is positive; black is out-of-plane and negative z component. Other colors demonstrate the orientation of the magnetization vector in-plane. Pair of antiferromagnetic (AFM) skyrmions located in the AFM interlayer exchange coupling (IEC) grain (1), in the ferromagnetic (FM) IEC grain (2) and single skyrmions (3,3*) fixed at the border of zero moiré potential in bottom and top layers, respectively. Boundaries with zero moiré potential are shown as white lines.

To demonstrate different types of skyrmion structures, Fig. 3 shows the configurations in the upper and lower layers of moiré magnet in this case. Pairs of coupled skyrmions can reside both in the AFM and FM IEC regions. In the first case (1), the total topological charge of the pair is equal to zero and, in the second (2), to two. Single skyrmions in one layer with a unit topological charge and domain walls in another layer are usually located in the region of zero moiré potential (3).

To explain the localization of skyrmions and domain walls near the boundaries of moiré grains, the energies of these structures near the boundaries $\Phi(\mathbf{r}) = 0$ were calculated. The results are shown in Fig. 4. We note that we only need to account for the interlayer exchange terms, which have explicit spatial dependence, while exchange and DMI terms are spatially invariant and, as thus, do not contribute to the domain wall localization. As a first step, we find the optimal position for the domain wall near zero moiré potential by varying its position along the line perpendicular to the grain boundary and calculating the energy of the system. It can be seen that, at a certain position, the energy is minimal, so this position is energetically favorable for the domain wall. It is also noticeable that this minimum is slightly offset from the point where $\Phi(\mathbf{r}) = 0$, which can be seen in Fig. 4.

The second step is to minimize the energy as function of the position of the skyrmion in the other layer. The wall in one layer retains its position, while the skyrmion in the other layer is translated in the direction perpendicular to the moiré grain boundary. There is also a certain energy minimum here which does not coincide with the minimum for the domain wall but is located closer to zero of the moiré potential.

III. SKYRMION DYNAMICS IN TWISTED MAGNETIC BILAYER

In this section, we will show that the three described types of skyrmions are characterized by the distinctive dynamics

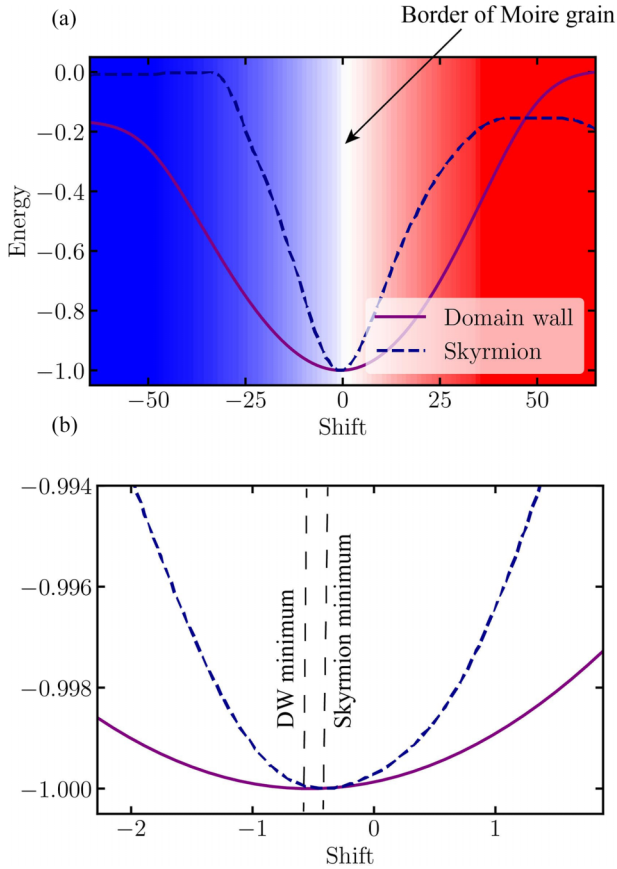


FIG. 4. Dependence of domain wall and skyrmion exchange energy (in a.u.) on the displacement with respect to the interlayer exchange potential (IEC) boundary. (a) Blue and red shaded areas correspond to the antiferromagnetic (AFM) and ferromagnetic (FM) IEC. (b) Zoomed central part presenting the shift of skyrmion and domain wall potential with respect to the grain boundary.

under applied spin-polarized current. We perform numerical simulation of the dynamics of the skyrmions using the LLG equation. At the same time, to provide a qualitative explanation of the specific features of the skyrmion dynamics, we employ collective coordinates and a generalization of the Thiele equation introduced in Ref. [33]. The Thiele equation was adapted to skyrmionic textures stabilized with DMI in Ref. [34], followed by Ref. [35] demonstrating weak interaction of the textures with impurities. In Refs. [36,37], the equation of motion for AFM skyrmions was derived demonstrating absence of the Hall angle. The AFM skyrmion pairs living in the moiré magnet consist of two ordinary skyrmions located in distinct layers, which is closer to SAFs than to single-layer materials with AFM exchange between nearest-neighbor atoms studied in Ref. [36]. The Thiele equation for SAFs is provided, e.g., in Ref. [38]. The interlayer exchange in the moiré magnets is variable in contrast to SAFs; the respective Thiele equations with necessary corrections are introduced below.

One of the features of moiré magnets is a domain wall localized in a single layer, which is pinned to the curve of zero interlayer exchange. As we have shown above, the skyrmions may attach to the domain wall; hence, the domain wall can be used as a guide for the skyrmions. It was proven in Ref. [39]

that the repulsive force between skyrmion and domain wall in the same layer can be used to enhance stability of the skyrmion and increase its speed. In moiré magnets, the domain wall and skyrmion are located in separate layers, and the skyrmion is attracted to the domain wall, resulting in an even greater stabilization effect, namely, for small DMI, single-layer skyrmions exist only in the vicinity of the domain walls.

Below, we provide a brief derivation of the Thiele equation for two-layer magnetic systems with varying interlayer exchange. In the Supplemental Material [40], we provide the results of the numerical simulation confirming that the collective coordinate approximation is valid.

A. Thiele equation

The dynamics of the bilayer system is described by the LLG equation:

$$\frac{d\mathbf{n}}{dt} = -\gamma\mathbf{n} \times \left(\mathbf{H}_{\text{eff}} - \eta M_s \frac{d\mathbf{n}}{dt} \right) + \tau, \quad (3)$$

where γ is gyromagnetic ratio, η is damping parameter, and \mathbf{H}_{eff} is the effective magnetic field:

$$\mathbf{H}_{\text{eff}} = -\frac{1}{M_s} \frac{\partial E}{\partial \mathbf{n}}. \quad (4)$$

All the vector fields depend on the layer $l = 1, 2$ and the spin coordinates $\mathbf{r} = (x, y)$. The term τ is the Slonczewski spin-transfer torque (STT) [41]:

$$\tau = -\mathbf{n} \times (\mathbf{n} \times \mathbf{j}_l) - \beta \mathbf{n} \times \mathbf{j}_l, \quad (5)$$

where β is the antidamping constant associated with STT, and

$$\mathbf{j}_l = (\mathbf{j} \cdot \nabla) \mathbf{n} = \sum_{k=x,y} j_k \frac{\partial \mathbf{n}}{\partial k}. \quad (6)$$

We are interested in the dynamics of the topological solitons, assuming their shape is invariant. Denote $\mathbf{R}^l = (R_x^l, R_y^l)$ the position of the soliton in layer l . If the shape is fixed, then \mathbf{R}^l 's are the only varying degrees of freedom. The constrained dynamics is derived by projecting the velocity $\dot{\mathbf{n}} = d\mathbf{n}/dt$ to the generators of the translations of the solitons:

$$\mathbf{G}_k^l = \frac{\partial \mathbf{n}_l}{\partial R_k^l} = -\frac{\partial \mathbf{n}_l}{\partial k}, \quad k = x, y. \quad (7)$$

The projected LLG equation onto the space spanned by the vectors \mathbf{G}_k^l is called the Thiele equation. For the multilayer system, the Thiele equation becomes

$$-4\pi Q^l J \dot{\mathbf{R}}^l = -\frac{\gamma}{M_s} \frac{\partial E}{\partial \mathbf{R}^l} + \gamma \eta M_s A^l \dot{\mathbf{R}}^l + 4\pi Q^l J \mathbf{j}^l + \beta^l A^l \mathbf{j}^l, \quad (8)$$

where Q^l is the topological charge of layer l :

$$Q^l = \frac{1}{4\pi} \int \mathbf{n}_l \cdot \left(\frac{\partial \mathbf{n}_l}{\partial x} \times \frac{\partial \mathbf{n}_l}{\partial y} \right) dr, \quad (9)$$

and we introduce matrices:

$$J = \begin{pmatrix} 0 & 1 \\ -1 & 0 \end{pmatrix}, \quad A_{jk}^l = \int \frac{\partial \mathbf{n}_l}{\partial j} \cdot \frac{\partial \mathbf{n}_l}{\partial k} dr, \quad j, k = x, y. \quad (10)$$

The Thiele equation can be solved with respect to $\dot{\mathbf{R}}$. Consider an FM pair of solitons; assuming their perfect alignment, then the system becomes essentially single layer with a thicker layer. Suppose the background phase is isotropic, e.g., FM; then $\partial E/\partial \mathbf{R} = 0$. The Thiele equation in this case is well known:

$$\dot{\mathbf{R}} = -(4\pi QJ + \gamma\eta M_s A)^{-1}(4\pi QJ + \beta A)\mathbf{j}. \quad (11)$$

The soliton velocity in this case is connected with current \mathbf{j} by a linear transform, and the transform commutes with rotations. Therefore, the angle between soliton velocity $\dot{\mathbf{R}}$ and current \mathbf{j} is constant and is called the Hall angle.

If the soliton is invariant under reflections with respect to both coordinate axes (e.g., skyrmion, skyrmionium), then matrix A is proportional to identity operator \hat{I} , $\hat{A} = A\hat{I}$. The Hall angle is given by

$$\theta = \pi + \arctan \frac{4\pi Q}{\beta A} - \arctan \frac{4\pi Q}{\gamma\eta M_s A}. \quad (12)$$

The Hall angle vanishes if (C1) $Q = 0$ or (C2) $\beta = \gamma\eta M_s$. The value of velocity is proportional to the current:

$$|\dot{\mathbf{R}}| = \left(\frac{16\pi^2 Q^2 + \beta^2 A^2}{16\pi^2 Q^2 + \gamma^2 \eta^2 M_s^2 A^2} \right)^{1/2} j. \quad (13)$$

In the case (C2), the velocity does not depend on the topological charge or dissipation constant. In the case $Q = 0$, the soliton velocity is given by

$$|\dot{\mathbf{R}}| = \frac{\beta}{\gamma\eta M_s} j \quad (14)$$

and is determined by the ratio of the damping constants.

Thus, the Thiele equation predicts that the skyrmions localized in the AFM domains will have no Hall angle due to the vanishing of the topological charge, and the sign of the Hall effect for the skyrmions in FM domains depends on the ratio of the Gilbert damping η and STT β . We will further confirm these predictions in the numerical simulations.

For the case when the skyrmion in one of the layers is in the vicinity of the domain wall in the other layer, one can also employ the Thiele equation. We assume rotational symmetry of the skyrmion (in practice, the symmetry can be slightly violated due to interaction with the domain wall). For clarity, we consider a flat grain boundary and straight domain wall, that is, the IEC potential Φ and the domain wall texture \mathbf{n}_2 depend only on the x coordinate. Energy of the system up to an additive constant is given by

$$V = -J_{1,2} \int \Phi(x) \mathbf{n}_1(x - R_x^1, y - R_y^1) \mathbf{n}_2(x - R_x^2) dx dy. \quad (15)$$

The magnetization M_s , the current j , and damping parameters η , β are assumed equal in both layers. The Thiele equation for the system is

$$\begin{aligned} \gamma\eta M_s A \dot{R}_x^1 + 4\pi Q \dot{R}_y^1 &= \frac{\gamma}{M_s} \frac{\partial V}{\partial R_x^1} - \beta A j_x - 4\pi Q j_y, \\ -4\pi Q \dot{R}_x^1 + \gamma\eta M_s A \dot{R}_y^1 &= 4\pi Q j_x - \beta A j_y, \\ \gamma\eta M_s b \dot{R}_x^2 &= \frac{\gamma}{M_s} \frac{\partial V}{\partial R_x^2} - \beta b j_x, \end{aligned} \quad (16)$$

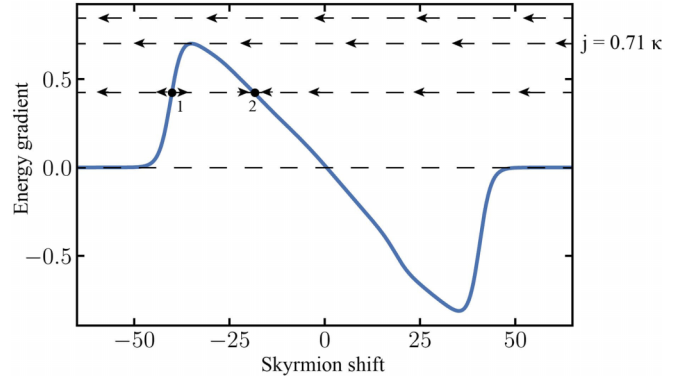


FIG. 5. The blue line defines the energy gradient as a function of skyrmion shift from the equilibrium position, which is actually the returning force. Energy profile, equilibrium position, and interaction potential are given in Fig. 4. To simplify the analysis of skyrmion motion, we consider the special case of the dissipation constants when the Hall angle vanishes: $\beta = \gamma\eta M_s$. In this case, the perpendicular force is produced only by j_x and by the potential gradient. Dashed horizontal lines demonstrate the absolute value of perpendicular current, given in the units of energy gradient. Arrows define the direction of skyrmion motion: we see that, for the current larger than critical value 0.71κ , the skyrmion leaves the boundary of the grain. For smaller currents, we obtain two equilibrium positions, one of which is sustainable, and the other one is unsustainable.

The first equation in Eq. (16) defines two competing forces, acting on a skyrmion on the grain boundary: the first one from potential gradient and the second one from the current. The raiting behavior of the skyrmion is observed for the values of perpendicular current less than some critical value, when the returning force can no longer compensate the action of the electric current, and the skyrmion leaves the grain boundary:

$$j_x^{cr} = \frac{\gamma^2 \eta A}{(4\pi Q)^2 + (\beta A)^2} \cdot \frac{\partial V}{\partial R_x^1} = \kappa \cdot \frac{\partial V}{\partial R_x^1}. \quad (17)$$

Here, we introduce the parameter κ :

$$\kappa = \frac{\gamma^2 \eta A}{(4\pi Q)^2 + (\beta A)^2}. \quad (18)$$

Figure 5 demonstrates the equilibrium points and critical current for the case of pinning to the rail.

We now check the predictions of the Thiele equation by numerical simulations via the LLG equation. The results of the simulations for the FM and AFM skyrmion pairs are shown in Fig. 6. The simulation was performed by evolving the initial state (labeled i.s. in the figures) for a fixed amount of time and taking the snapshot of the final state. The simulation was performed for three different values of the antidamping constant β . First, it is seen that, for the AFM skyrmion pair with zero topological charge, the Hall angle vanishes, and the skyrmion propagates along the current according to Eq. (12). Moreover, the module of velocity grows linearly with β as follows from Eq. (13). For the case of the FM skyrmion, the Hall angle is generally finite and depends on the ratio between antidamping constant β and Gilbert damping constant η .

For the single-layer skyrmion localized in the vicinity of the domain wall in the other layer, the LLG simulations

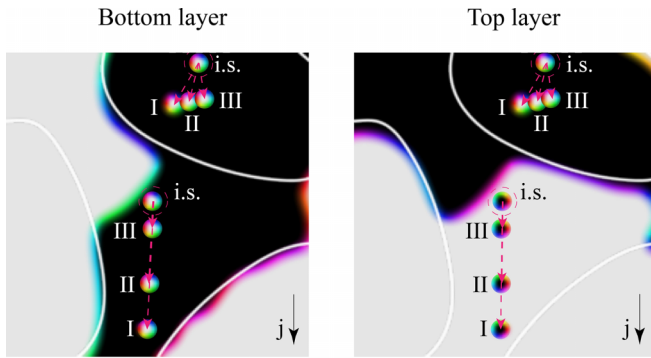


FIG. 6. Dynamics of skyrmion pairs for different values of β . The temporal evolution of skyrmion positions over an identical period of time is demonstrated. i.s. = initial state, I: final state for $\beta = 0.6$, II: $\beta = 0.45$, III: $\beta = 0.15$. The value of Gilbert damping constant η here equals 0.2. The color scheme description is the same as in Fig. 3.

are shown in Fig. 7. In the figure, two skyrmions can be identified localized in two different layers. It can be seen that, for the bottom-layer skyrmion, the angle between the current direction and the domain wall is relatively small, and thus, the skyrmion propagates along the domain wall. At the same time, for the top-layer skyrmion, the current is almost perpendicular to the domain wall, and thus, the skyrmion is dragged away from the domain wall and then disappears. This behavior qualitatively corresponds to the predictions of the Thiele in Eq. (17). As can be seen, the Thiele equation gives qualitatively correct predictions for the dynamics of the three types of skyrmions. This is due to the fact that, as we show in Appendix C, the skyrmion profile indeed remains almost unaffected in the course of motion under applied current. At the same time, there are quantitative discrepancies between the numerical modeling and analytical simulations which are caused by the smooth variations of the moiré potential along the domain wall, the presence of skyrmionic internal degrees of freedom which may cause its inertia, and the offset of the initial skyrmion position with respect to the bottom of the potential produced by the domain wall, which may affect the

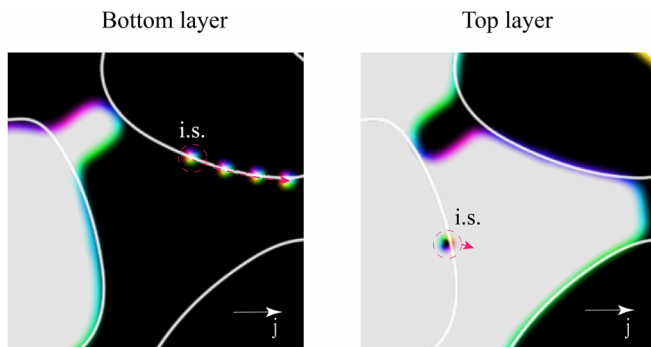


FIG. 7. Motion of skyrmion along the domain wall. i.s. = initial state. The color scheme description is the same as in Fig. 3. Single skyrmions tend to be located in the area of zero interlayer interaction potential (borders of moiré grains). If current direction makes not too large an angle with the direction of the grain boundary, the skyrmion remains attached to this boundary in the process of movement and moves along a kind of rail.

numerically extracted value of the threshold current. We also note that there exists a considerably larger threshold current needed to depin the domain wall from the moiré potential boundary. However, for the currents close to the threshold current for the skyrmion depinning, the domain walls remained pinned to the grain boundary.

IV. CONCLUSIONS

We have shown that the interplay of the spatially dependent interlayer moiré exchange potential and DMI in vdW magnets leads to a rich variety of noncollinear magnetic structures. Specifically, we have identified three distinct families of skyrmions characterized by different topological properties and kinetics under applied in-plane current. Of particular interest are the skyrmions pinned to the grain boundary of the moiré potential. Our numerical calculations predict the railing of these skyrmions along the grain boundary under applied current, and we have provided an analytical description of this effect using the Thiele equation. This behavior is quite general for the two-layer structures with spatially varying interlayer exchange potential, and we thus anticipate that it may be observed in different vdW moiré magnetic bilayers. We note that the moiré potential-induced domain walls are pinned and are not moving with the external current. Therefore, engineering the twist in vdW structures can allow us to shape the flow of skyrmions in a predefined way along the domain wall boundaries. Railing of skyrmions in vdW magnets opens routes toward applications of these heterostructures in spintronics.

ACKNOWLEDGMENTS

This paper was supported by the Russian Science Foundation Grant No. 22-22-00632 [42].

APPENDIX A: NONCOLLINEAR MAGNETIC PHASES IN TWISTED MAGNETIC BILAYER

Figure. 8 provides the evolution of noncollinear phases, stabilized in moiré magnets for different values of ζ . The dimensionless parameter $\zeta = D/D_s$.

More detailed consideration of magnetization for $\zeta = 10$ is given in Fig. 9. The structure obtained in that case is the so-called fingerprint pattern. The small points that manifest in the regions characterized by AFM exchange coupling are subjected to a detailed investigation. These defects emerge at the intersections of domains (fingers), as visually exemplified in the figure.

APPENDIX B: STABILITY OF SKYRMION

To discover the applicability of the Thiele equation in our analysis, we examine the deformation of the skyrmion profile, as depicted in Fig. 10.

Notably, the skyrmion profile remains predominantly unchanged and retains its symmetry while moving along the domain wall. However, once the skyrmion starts leaving the boundary and begins to collapse, deformation becomes evident. Based on these observations, we infer that the Thiele equation holds validity during the stable motion of the skyrmion.

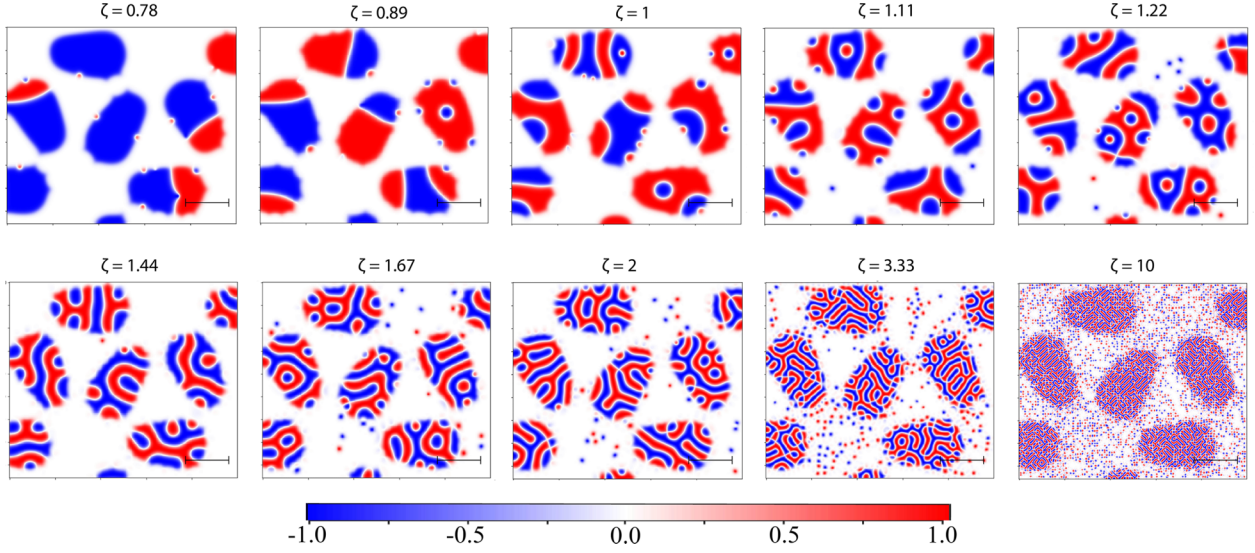


FIG. 8. z projection of total bilayer magnetic moments in moiré magnets for different values of ζ . Scale bar: 100 lattice constants.

APPENDIX C: CRITICAL CURRENT CONDITION

Consider the system of equations obtained for the case of the skyrmion and domain wall interaction:

$$\begin{aligned} \gamma\eta M_s A \dot{R}_x^1 + 4\pi Q \dot{R}_y^1 &= \frac{\gamma}{M_s} \frac{\partial V}{\partial R_x^1} - \beta A j_x - 4\pi Q j_y, \\ -4\pi Q \dot{R}_x^1 + \gamma\eta M_s A \dot{R}_y^1 &= 4\pi Q j_x - \beta A j_y, \\ \gamma\eta M_s b \dot{R}_x^2 &= \frac{\gamma}{M_s} \frac{\partial V}{\partial R_x^2} - \beta b j_x. \end{aligned} \quad (C1)$$

$$E = 0.1 \quad D = 0.9 \quad K = 0.01$$

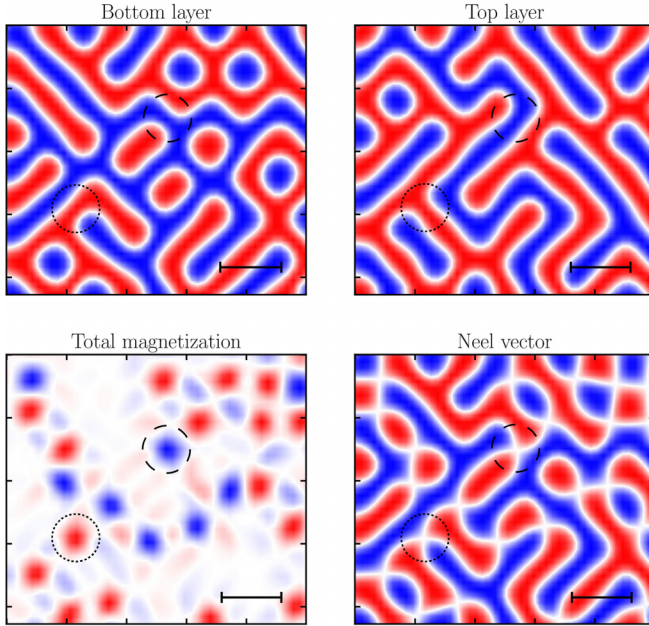


FIG. 9. Normalized z projection of magnetic moments for $\zeta = 10$. Magnetization in the first layer, second layer, total magnetization (the sum of the magnetizations of the first and second layers at a given point), and Néel vector (the difference between the magnetizations of the first and second layers) are given. Scale bar: 10 lattice constants.

Consider the first two equations that relate to the first layer. We focus on the special case in which the Hall angle vanishes and the skyrmion tends to move along the current (this regime is provided by the special relation between the parameters $\beta = \gamma\eta M_s$). Following this, the equations get the form:

$$\begin{aligned} \beta A \dot{R}_x^1 + 4\pi Q \dot{R}_y^1 &= \frac{\gamma}{M_s} \frac{\partial V}{\partial R_x^1} - \beta A j_x - 4\pi Q j_y, \\ -4\pi Q \dot{R}_x^1 + \beta A \dot{R}_y^1 &= 4\pi Q j_x - \beta A j_y, \end{aligned} \quad (C2)$$

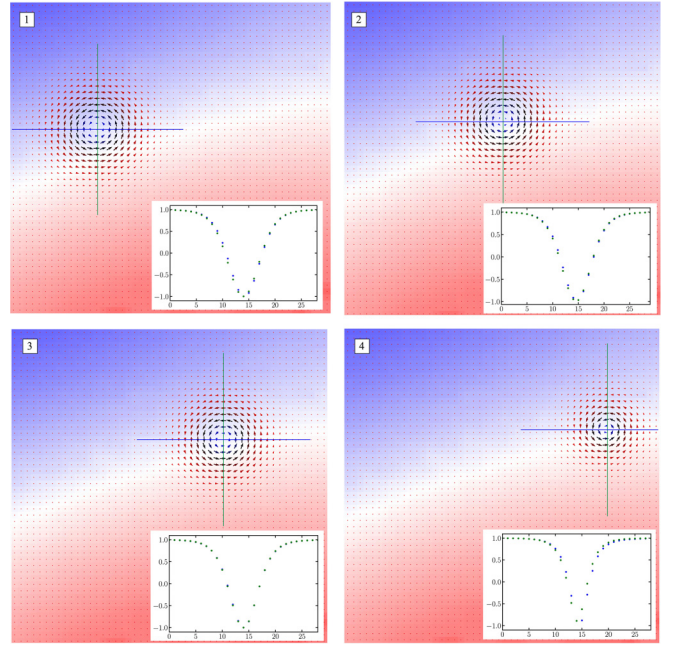


FIG. 10. Modification of the skyrmion profile as it moves along the domain wall. Insets show two cross-sections of the z component of the skyrmion magnetization along the lines of corresponding color.

$$\dot{R}_y^1 = \frac{4\pi Q}{\beta A} (j_x + \dot{R}_x^1) - j_y,$$

$$\dot{R}_x^1 = \frac{\gamma}{M_s \beta A} \cdot \frac{\partial V}{\partial R_x^1} - j_x - \frac{4\pi Q}{\beta A} \dot{R}_y^1 - \frac{4\pi Q}{\beta A} j_y, \quad (\text{C3})$$

$$\dot{R}_x^1 = \frac{\gamma \beta A}{M_s [(4\pi Q)^2 + (\beta A)^2]} \cdot \frac{\partial V}{\partial R_x^1} - j_x. \quad (\text{C4})$$

The condition for the critical current (the value of current when the returning force does not compensate the current any more and the skyrmion leaves the boundary) is $\dot{R}_x^1 = 0$. Here, we introduce the parameter κ :

$$j_x^{cr} = \frac{\gamma^2 \eta A}{(4\pi Q)^2 + (\beta A)^2} \cdot \frac{\partial V}{\partial R_x^1} = \kappa \cdot \frac{\partial V}{\partial R_x^1}. \quad (\text{C5})$$

- [1] Y. Liu, N. O. Weiss, X. Duan, H.-C. Cheng, Y. Huang, and X. Duan, Van der Waals heterostructures and devices, *Nat. Rev. Mater.* **1**, 16042 (2016).
- [2] K. S. Novoselov, O. A. Mishchenko, O. A. Carvalho, and A. H. Castro Neto, 2D materials and van der Waals heterostructures, *Science* **353**, aac9439 (2016).
- [3] K. S. Burch, D. Mandrus, and J.-G. Park, Magnetism in two-dimensional van der Waals materials, *Nature (London)* **563**, 47 (2018).
- [4] M. Blei, J. Lado, Q. Song, D. Dey, O. Erten, V. Pardo, R. Comin, S. Tongay, and A. Botana, Synthesis, engineering, and theory of 2D van der Waals magnets, *Appl. Phys. Rev.* **8**, 021301 (2021).
- [5] B. Huang, G. Clark, E. Navarro-Moratalla, D. R. Klein, R. Cheng, K. L. Seyler, D. Zhong, E. Schmidgall, M. A. McGuire, D. H. Cobden *et al.*, Layer-dependent ferromagnetism in a van der Waals crystal down to the monolayer limit, *Nature (London)* **546**, 270 (2017).
- [6] C. Gong, L. Li, Z. Li, H. Ji, A. Stern, Y. Xia, T. Cao, W. Bao, C. Wang, Y. Wang *et al.*, Discovery of intrinsic ferromagnetism in two-dimensional van der Waals crystals, *Nature (London)* **546**, 265 (2017).
- [7] S. Yang, T. Zhang, and C. Jiang, van der Waals magnets: Material family, detection and modulation of magnetism, and perspective in spintronics, *Advanced Science* **8**, 2002488 (2021).
- [8] S. Jiang, J. Shan, and K. F. Mak, Electric-field switching of two-dimensional van der Waals magnets, *Nat. Mater.* **17**, 406 (2018).
- [9] H. Polshyn, J. Zhu, M. A. Kumar, Y. Zhang, F. Yang, C. L. Tschirhart, M. Serlin, K. Watanabe, T. Taniguchi, A. H. MacDonald *et al.*, Electrical switching of magnetic order in an orbital Chern insulator, *Nature (London)* **588**, 66 (2020).
- [10] S. Jiang, L. Li, Z. Wang, K. F. Mak, and J. Shan, Controlling magnetism in 2D CrI₃ by electrostatic doping, *Nat. Nanotechnol.* **13**, 549 (2018).
- [11] T. Li, S. Jiang, N. Sivadas, Z. Wang, Y. Xu, D. Weber, J. E. Goldberger, K. Watanabe, T. Taniguchi, C. J. Fennie *et al.*, Pressure-controlled interlayer magnetism in atomically thin CrI₃, *Nat. Mater.* **18**, 1303 (2019).
- [12] Y. Qi, M. A. Sadi, D. Hu, M. Zheng, Z. Wu, Y. Jiang, and Y. P. Chen, Recent progress in strain engineering on van der Waals 2D materials: Tunable electrical, electrochemical, magnetic, and optical properties, *Adv. Mater.* **35**, 2205714 (2023).
- [13] R. Jaeschke-Ubiergo, E. Suarez Morell, and A. S. Nunez, Theory of magnetism in the van der Waals magnet CrI₃, *Phys. Rev. B* **103**, 174410 (2021).
- [14] A. K. Behera, S. Chowdhury, and S. R. Das, Magnetic skyrmions in atomic thin CrI₃ monolayer, *Appl. Phys. Lett.* **114**, 232402 (2019).
- [15] W. Chen, Z. Sun, Z. Wang, L. Gu, X. Xu, S. Wu, and C. Gao, Direct observation of van der Waals stacking-dependent interlayer magnetism, *Science* **366**, 983 (2019).
- [16] N. Sivadas, S. Okamoto, X. Xu, C. J. Fennie, and D. Xiao, Stacking-dependent magnetism in bilayer CrI₃, *Nano Lett.* **18**, 7658 (2018).
- [17] Q. Tong, F. Liu, J. Xiao, and W. Yao, Skyrmions in the moiré of van der Waals 2D magnets, *Nano Lett.* **18**, 7194 (2018).
- [18] B. Huang, M. A. McGuire, A. F. May, D. Xiao, P. Jarillo-Herrero, and X. Xu, Emergent phenomena and proximity effects in two-dimensional magnets and heterostructures, *Nat. Mater.* **19**, 1276 (2020).
- [19] T. Song, Q.-C. Sun, E. Anderson, C. Wang, J. Qian, T. Taniguchi, K. Watanabe, M. A. McGuire, R. Stöhr, D. Xiao *et al.*, Direct visualization of magnetic domains and moiré magnetism in twisted 2D magnets, *Science* **374**, 1140 (2021).
- [20] C. Xu, J. Feng, S. Prokhorenko, Y. Nahas, H. Xiang, and L. Bellaïche, Topological spin texture in Janus monolayers of the chromium trihalides Cr(I, X)₃, *Phys. Rev. B* **101**, 060404(R) (2020).
- [21] F. Xiao, K. Chen, and Q. Tong, Magnetization textures in twisted bilayer CrX₃ (X = Br, I), *Phys. Rev. Res.* **3**, 013027 (2021).
- [22] Y. H. Kwan, G. Wagner, N. Bultinck, S. H. Simon, and S. A. Parameswaran, Skyrmions in twisted bilayer graphene: Stability, pairing, and crystallization, *Phys. Rev. X* **12**, 031020 (2022).
- [23] F. Zheng, Magnetic skyrmion lattices in a novel 2D-twisted bilayer magnet, *Adv. Funct. Mater.* **33**, 2206923 (2023).
- [24] R. A. Duine, K. J. Lee, S. S. P. Parkin, and M. D. Stiles, Synthetic antiferromagnetic spintronics, *Nat. Phys.* **14**, 217 (2018).
- [25] J. Unguris, R. J. Celotta, and D. T. Pierce, Observation of two different oscillation periods in the exchange coupling of Fe/Cr/Fe(100), *Phys. Rev. Lett.* **67**, 140 (1991).
- [26] W. Legrand, D. Maccariello, F. Ajejas, S. Collin, A. Vecchiola, K. Bouzehouane, N. Reyren, V. Cros, and A. Fert, Room-temperature stabilization of antiferromagnetic skyrmions in synthetic antiferromagnets, *Nat. Mater.* **19**, 34 (2020).
- [27] K. V. Voronin, I. S. Lobanov, and V. M. Uzdin, Activation energy and mechanisms for skyrmion collapse in synthetic antiferromagnets, *JETP Lett.* **116**, 240 (2022).
- [28] Y. Xu, A. Ray, Y.-T. Shao, S. Jiang, K. Lee, D. Weber, J. E. Goldberger, K. Watanabe, T. Taniguchi, D. A. Muller *et al.*, Coexisting ferromagnetic-antiferromagnetic state in twisted bilayer CrI₃, *Nat. Nanotechnol.* **17**, 143 (2022).
- [29] Q. H. Wang, A. Bedoya-Pinto, M. Blei, A. H. Dismukes, A. Hamo, S. Jenkins, M. Koperski, Y. Liu, Q.-C. Sun, E. J. Telford *et al.*, The magnetic genome of two-dimensional van der Waals materials, *ACS Nano* **16**, 6960 (2022).

- [30] K. Hejazi, Z. X. Luo, and L. Balents, Noncollinear phases in moiré magnets, *Proc. Natl. Acad. Sci. USA* **117**, 10721 (2020).
- [31] A. Otero Fumega and J. Lado, Moiré-driven multiferroic order in twisted CrCl₃, CrBr₃ and CrI₃ bilayers, *2D Mater.* **10**, 025026 (2023).
- [32] I. S. Lobanov and V. M. Uzdin, The lifetime of micron scale topological chiral magnetic states with atomic resolution, *Comput. Phys. Commun.* **269**, 108136 (2021).
- [33] A. A. Thiele, Steady-state motion of magnetic domains, *Phys. Rev. Lett.* **30**, 230 (1973).
- [34] K. Everschor, M. Garst, R. A. Duine, and A. Rosch, Current-induced rotational torques in the skyrmion lattice phase of chiral magnets, *Phys. Rev. B* **84**, 064401, (2011).
- [35] J. Iwasaki, M. Mochizuki, and N. Nagaosa, Universal current-velocity relation of skyrmion motion in chiral magnets, *Nat. Commun.* **4**, 1463 (2013).
- [36] E. G. Tveten, A. Qaiumzadeh, O. A. Tretiakov, and A. Brataas, Staggered dynamics in antiferromagnets by collective coordinates, *Phys. Rev. Lett.* **110**, 127208 (2013).
- [37] J. Barker and O. A. Tretiakov, Static and dynamical properties of antiferromagnetic skyrmions in the presence of applied current and temperature, *Phys. Rev. Lett.* **116**, 147203 (2016).
- [38] K. Wang, V. Bheemarasetty, and G. Xiao, Spin textures in synthetic antiferromagnets: Challenges, opportunities, and future directions, *APL Mater.* **11**, 070902 (2023).
- [39] X. Xing, J. Akerman, and Y. Zhou, Enhanced skyrmion motion via strip domain wall, *Phys. Rev. B* **101**, 214432 (2020).
- [40] See Supplemental Material at <http://link.aps.org/supplemental/10.1103/PhysRevB.108.174440> for the animations illustrating skyrmion dynamics under applied current.
- [41] J. C. Slonczewski, Conductance and exchange coupling of two ferromagnets separated by a tunneling barrier, *Phys. Rev. B* **39**, 6995 (1989).
- [42] <https://rscf.ru/en/project/22-22-00632/>.